*Gazi University Journal of Science*
*GU J Sci*
*28(3):365-375 (2015)*

# Defect Research of InGaN Based on Blue LED Structures Using Reciprocal Space Mapping

Y. BAŞ[1], M. TAMER[2], A. GÜLTEKİN[3], M.K. ÖZTÜRK[3,♠], H. ALTUNTAŞ[4], S. ÖZÇELIK[3], E. ÖZBAY[5]

[1]*National Boron Research Institute, Ankara, Turkey*
[2]*Faculty of Education, Zirve University, Gaziantep, Turkey*
[3]*Department of Physics, Gazi Photonic Research Center, Ankara, Turkey*
[4]*Department of Physics, Karatekin University, Çankırı, Turkey*
[5]*Nanotechnology Research Center, Department of Physics, Department of Electrical and Electronics Engineering, Bilkent, 06800, Ankara, Turkey*

*Received: 09/02/2015 Revised: 22/04/2015 Accepted: 02/06/2015*

**ABSTRACT**

Between n- GaN and p- AlGaN+GaN contacts, the blue light emitting diode (LED) structure with InGaN/GaN multiple quantum well has been grown using metalorganic vapor phase epitax (MOCVD) on c-oriented sapphire substrate. In order to research the strain and the stress of the lattice in crystal form, a reciprocal lattice space was mapped using a High Resolution X-Ray Diffractometer. In this study, by taking the qualities of the GaN epitaxial structure as reference point; relaxation, strain, hydrostatical strain and biaxial strain parameters are researched for the point defects taking the increasing temperatures into consideration. All parameters except the growth temperature of the InGaN layer were kept fixed for all samples. Depending on the growth temperature values, the results indicated a monotonous increasing-decreasing or decreasing-increasing manner. Additionally, the point defects of the blue LED structure on AlGaN layer have been compared to those of InGaN layer. While the lattice relax exchange of both layers were behaving in an opposite manner to each other; hydrostatic and biaxial strain exchanges were behaving in a parallel manner for both layers. As a result, since the points and the defects were carried from one layer to the other, the same tendencies were observed.

**Keywords:** Blue LED, MOCVD, HRXRD, Point defect

## 1. INTRODUCTION

Today, Group III nitrogen based semi-conductors are commonly used in industrial area due to their visible spectral region. LED telephone screens, computer monitors and billboards have become an integral part of everyday life. Especially, functioning of the semi-conductor LEDs on short wavelengths, their emitting strong radiation on red, green and blue colors and on high luminescence, and more importantly their being noticed from afar add to the significance of these devices [1]. These can be grown epitaxially through MOCVD. The most common problem with the LED structures that has been grown with MOCVD system is the formation of various point defects when elements such as oxygen (O), nitrogen (N) and gallium (Ga) enter the system as impurities. [2,3]. These defects can be listed as; substitution (when the Ga atom is replaced with Aluminum (Al) atom), interstitial point defect, forming lattice expansion or compression depending on the covalent radius (e.g. the different local clustered domains are occurred entering between lattices of N, Ga

♠Corresponding author, e-mail: ozturkm@gazi.edu.tr

and Al, which causes the cracks with dislocation density in crystal.) and the formation of vacancies (when the places of Al, Indium (In) and Ga are blank and formed a crystal lattice compression) [4]. As the interposing of elements with bigger covalent radii to elements with smaller covalent radii, and the formation of the vacancies cause strain on the crystal lattices, the opposite causes volumetrical growth of the crystal lattices. The point defects lead to changes in the optical stimulations and the electrical properties through the fluctuation of the improving conditions and these defects attract still attention for new material research in the literature. Nakamura clearly stated that the performance of many traditional optoelectronic devices could be enhanced through the controlling of the point defects and the structural defects [5]. Moreover, GaN and AlN tampons or contact layers often grow in large mosaic crystal structure [6,7]. The primary cause of the case is the lattice mismatch of the sapphire substrate, which is up to 23% within these layers [8]. In a hetero-structure, even the moving of the dislocations to the top layer can be observed. The lattice mismatches reveal the dislocations in the layer and these dislocations cause a leakage current of a considerable portion [9]. The leakage current, yellow photo-stimulation and non-active format status limit the lifespan and the performance of the device substantially [10-12]. Despite the existence of strain-related dislocations, GaN hetero epitaxial films are under significant strain. Strains, which affect the electronic band structure and the luminescence [13], are often associated with the splitting and the twisting of the films [14]. In addition to all that is listed, strains are also the driving force behind the relations of the structure defects and their formatting.

In this article, the three blue InGaN MQW LED structures grown by MOCVD technique were examined in high quality crystal structure. In order to acquire a detailed structural analysis, the reciprocal lattice space of the InGaN based MQW blue LED structure has been mapped. During the mapping, a cubical equation has been used to calculate the changed In ratio and it has been followed up with the calculations of the lattice strain and components. After the a- and c- lattice parameters of the grown LEDs has been figured out definitively, the point defects (relax, strain, biaxial strain, hydrostatical strain and stress) has been researched in accordance with the increasing temperature of the InGaN active layer in order to find the detailed crystal structure defects; and the associations between these qualities have been discussed.

## 2. EXPERIMENTAL DETAILS

### 2.1. Material preparation

Prior to the growth process, as preparation, sapphire ($Al_2O_3$) substrate has been cleaned with $H_2$ gas at 1100 $^oC$. MOCVD technique has been employed for all growth procedures. Firstly, the GaN core level on sapphire substrate has been grown at 500 $^oC$. Later on, the GaN tampon layer has been grown to a thickness of 25 nm. The pressure has been kept stable at 200 mbar during the procedures. Afterwards, the n-type GaN contact layers has been grown at 1030 $^oC$ with 23 sccm Trimethylgallium (TmGa) constant flux as the growth of the first layer lasted 35 minutes and the second layer lasted 20 minutes. In the following step, InGaN/GaN MQW layer has been grown at the140 sccm TeGa and Trimetilindium (TmIn) flux ratings to achieve the desired five layers for 90 and later on for 390 seconds. On MQW, the GaN top layer has been grown for 390 seconds at a flux rating of 140 sccm TeGa at 730 $^oC$. As the top layer, magnesium extrinsic p-contact AlGaN layer was grown for the flux ratings of 9 sccm TmGa, 15 sccm Trimethylaluminium (TmAl) and 90 sccm Bis (siklopentadienil) magnesium at 50 mbar pressure with 1085 $^oC$, and as the bottom layer it has been grown with the flux ratings of 14 sccm TmGa and 100 sccm $Cp_2Mg$ for 720 seconds at 200 mbar pressure and at 1010 $^oC$. The $NH_3$ flux rating has been adjusted at 1300 sccm for GaN and AlGaN layers and at 5200 sccm for InGaN/GaN active layers. The active layer growth temperatures for these three samples are 650 $^oC$, 667 $^oC$ and 700 $^oC$. The growth conditions of the other layers have been kept stable for all the samples. Structural diagram of InGaN LEDs is shown in Figure 1.

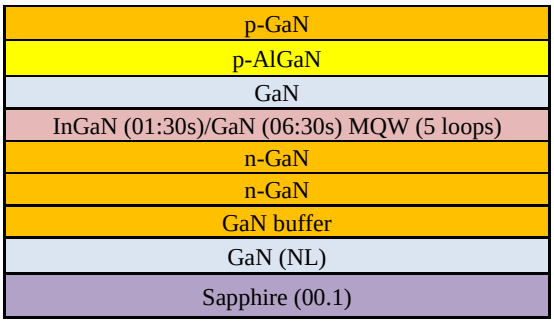


Figure 1. Structural diagram of the InGaN LEDs

The HRXRD measurements have been taken with the D8-Discovery XRD and a 1.5406-Å-wavelenght $CuK\alpha_1$ tube has been used as the source. To achieve the desired high resolution, a 4-crystal Ge (220) crystallized monochromator was preferred. In order to provide the diffraction conditions of symmetrical-assymmetrical planes; x, y, z, Φ and ξ axes are present in addition to the θ and 2θ axes. x, y, z, Φ and ξ axes are preferred for the reciprocal lattice space mapping. The samples were affixed to the device with vacuum. Additionally, during the optimization of the reciprocal lattice space mapping, the average shooting time for each measurement (with the axes) was 7 hours, leading to an approximate 112 hours of shooting time in total.

## 3. RESULTS AND DISCUSSIONS

In order to research the crystal structure defects of the blue LED samples, reciprocal lattice space mapping through the HRXRD technique can be used. In the previous studies, the rocking curve obtained through the θ scanning fixed with 2θ diffraction angle on diffraction plane is often employed [14-16]. However, there are

many factors taken into consideration at the optimization of the rocking curve. Among these factors, the adjustment of the height, surface curvature and azimuth adjustment play a crucial role. By optimizing the device settings crystallographically, the peak angle with the error margins caused by the same factors triggering the diffraction effect, the distance between planes and the lattice parameters could be obtained with precise results. However, in order to calculate these parameters more precisely, it is better to use the reciprocal lattice space mapping as it is obtained through slower scanning steps when the crystallographical adjustment is done properly. In a reciprocal lattice space map, the plane peak can be observed in all its details clearly. The plane reflection peak creates an imperfect image on the asymmetrical plane by digressing from the original peak in the diffraction curve. The word "asymmetry" here is not to be misunderstood. When the X-rays are fully reflected on the planes, the peak that makes a symmetrical entry can be observed. However, due to the defects of the sample, this occasionally results in the formation of a diffraction pattern, when the asymmetrical peak loses impetus, and symmetry, leading to misinterpretations of the analysis of the sample. As a result, it can be concluded that it is possible to research the crystal structure defects with more precise results through the reciprocal lattice space mapping method, and the indium (In) ratios of the InGaN layers of both symmetrical and asymmetrical planes can be calculated more accurately.

Changing the In ratio in InGaN/GaN MQW structures create single color, high-resolution spectra in the visible spectrum. When the In ratios are high, they create drops of In, leading to an increase of the crystal structure defects of the structures and affecting the structure negatively. However, when the In ratios are low, it causes a better optimization of the growth conditions and overlapping entries in the HRXRD analysis.

Peaks, which have entries in such a manner, generally have point defects; while the number of the satellite peaks that have thickness entries dwindle, they affect the finger peaks caused by the roughness. Figure 2 shows the reciprocal lattice space mapping of MQW blue LED sample's symmetrical (0002) and asymmetrical (10-15) planes for sample B. In the (0002) and (10-15) 2theta-omega reciprocal lattice space map, AlGaN, GaN and InGaN peaks can be seen in a consecutively decreasing angle. On Plane (0002), GaN and InGaN peak reflections overlap, while the GaN and InGaN peak entries are slightly separated on Plane (10-15). Moreover, there are two satellite peaks in addition to the layers. These satellite peaks are used to find the quantum well thickness. On the asymmetrical planes, it could be observed that one of the satellite peaks is weaker.

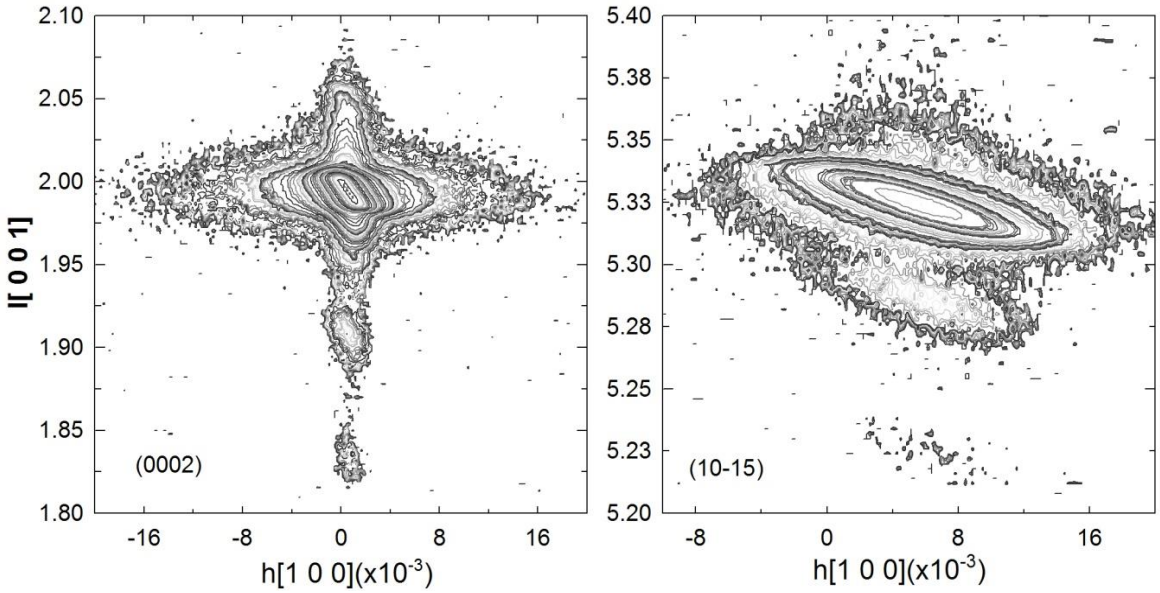


**Figure 2.** The reciprocal lattice space mapping of LED MQW sample's symmetrical (0002) and asymmetrical (10-15) planes for sample B. (InGaN layer has been grown at 667 $^{o}$C)

To represent all scans, the peak positions and the half-widths of the peak heights of planes (0002), (0004), (0006) and (10-15) have been provided at Figure 3. Hence, it was possible to show the FWHM values of the InGaN and AlGaN layers separately. 0.15$^{o}$ has been added to the AlGaN FWHM values. For Samples B and C, firstly an increase or a decrease, and later on a decrease or an increase can be observed on the symmetrical planes depending on the angle. However, Sample A shows an increase in the FWHM values. In the meantime, in all three samples AlGaN layer shows a tendency to increase or decrease in the beginning, followed by a decrease and an increase depending on the angle.

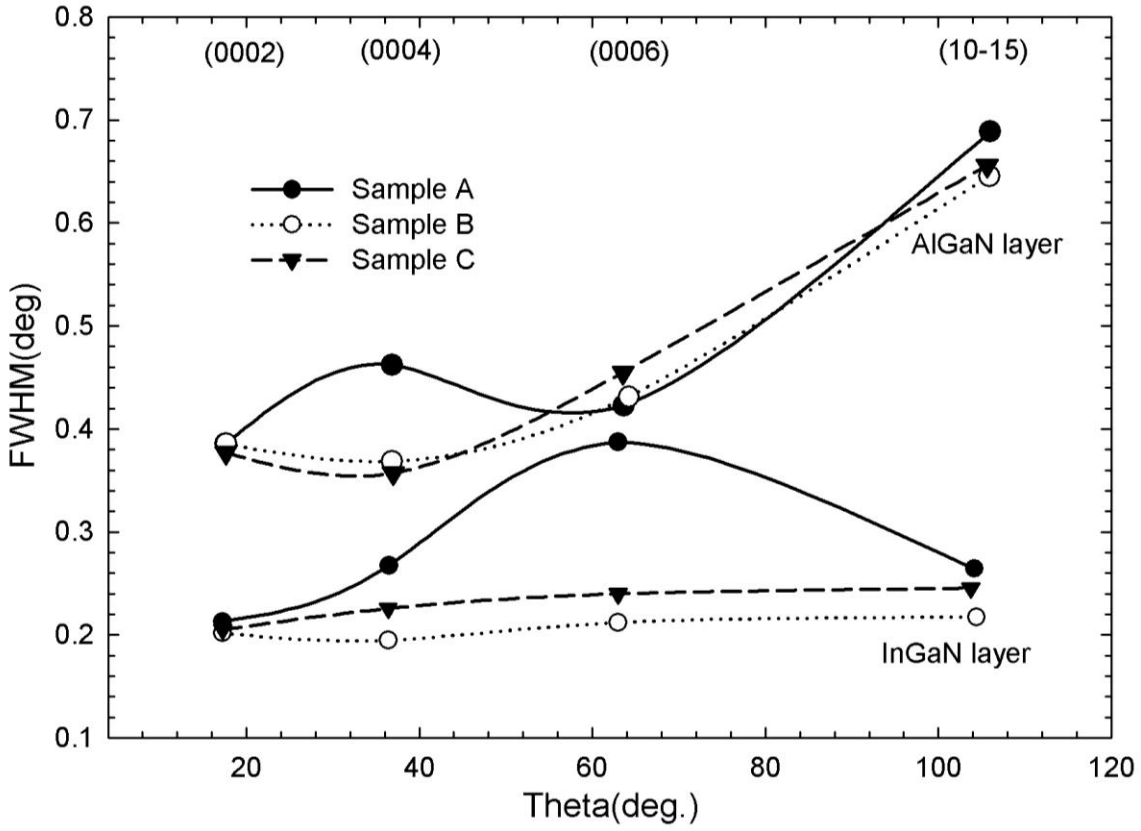


**Figure 3.** The FWHM values of (0002), (0004), (0006) (10-15) InGaN and AlGaN Layers depending on the Bragg Diffraction Angles for Samples A, B and C.

On Figure 3, the FWHM values for all three samples can be compared on the same plane. As a result, while Samples C, B and A display quite close increase sequencing on plane (0002) of InGaN layer in terms of FWHM values, they can be observed to display a more differentiated increase sequencing on diffraction planes (0004) and (0006). Also the asymmetrical plane of the InGaN is in accordance with this sequencing. For all three samples, there was a small FWHM difference in the sequencing of C, B and A Samples consecutively on the AlGaN Symmetrical Plane (0002); however, on Plane (0004) the difference of the FWHM values are more discernible and the FWHM value of Sample A is higher, compared to those of plane (0002). On Plane (0006), the FWHM differences are quite minute, just like those of plane (0002), but the sequencing is reversed compared to planes (0002) and (0004). On AlGaN Asymmetrical plane (10-15), on the other hand, a low FWHM difference and an increasing sequencing of Samples B, C and A can be observed just like planes (0002) and (0006).

In order to separate $k\alpha_1$ and $k\alpha_2$ in the parallel beam and to eliminate $k\alpha_2$ in the HRXRD technique, Ge 022 (+, - , - , +) monochromator and Göebbels mirror were employed. The measurements of the symmetrical and asymmetrical reflections, Bragg Angle θ and lattice curving angle $\tau$ can be calculated through the $\theta = (\theta_+ + \theta_-)/2$ and $\tau = (\theta_+ - \theta_-)/2$ equations [17]. *a* and *c* lattice parameters of corrupted InGaN hexagonal unit cell are calculated from a proper angle of the hk(-h-k)l reflection. Three different techniques could be employed to calculate the lattice. For the first technique, the lattice parameter of the InGaN, by taking the Vegard Law into consideration, is found by adding *x* numbered InN lattice parameters to (1-x) numbered GaN lattice parameters. The values found are given at the 3rd and the 6th columns of Table 1 for both InGaN and AlGaN. When the increasing growth temperature is considered, *c* lattice parameter behaves in a decreasing manner on InGaN layer in picometer level while AlGaN layer behaves in a manner that shows an initial increase followed by a decrease in accordance with the values calculated through Vegard Law. With the increase of the growth temperature, *a* values calculated through Vegard Law, behave in a manner that shows an initial increase followed by a decrease for InGaN layer, and they behave in an increasing manner for AlGaN layer. In order to obtain *a* and *c* lattice parameters on the asymmetrical planes, by means of using $Sin\tau$ and $Cos\tau$ at the denominator of the equations below, the second technique is determined with below equations [18].

$$c = \frac{\lambda l}{2\,Sin\,\theta\,Cos\,\tau} \quad (1)$$

$$a = \frac{\lambda\sqrt{4/3}\sqrt{h^2+hk+k^2}}{2\,Sin\,\theta\,Sin\,\tau} \quad (2)$$

At the second technique, depending on the increasing growth temperature, *c* values behave in a decreasing manner on the picometer level on the InGaN layer while they behave in a manner that shows an initial increase followed by a decrease for AlGaN layer, paralleling the results with the calculations to those based on the Vegard Law. On the other hand, A levels shows a decreasing behavior on the picometer level of the InGaN layer, and they show an initially increasing and later on decreasing behavior for the AlGaN layer.

For the last technique, by means of using the $(1-D\,Cos^2\theta)\,/\,(r\,Sin\,\theta)$ error function and Bragg Law, the lattice parameters could be calculated by;

$$c = \frac{l\,\lambda}{2Sin\theta}\,x\left(error\ \ function\right) \quad (3)$$

$$a^{(hkl)} = c\,d_{hkl}\sqrt{\frac{(4/3)\left(h^2+k^2+hk\right)}{c^2-l^2d_{hkl}^2}} \quad (4)$$

(3) and (4) equations [19]. On the error function, *D* is the possible dislocation of the sample with goniometer axis on asymmetrical plane (equatorial plane) and its value is 0.02. The r value, which is the distance of the sample from the detector, is 450 nm. The *c* values, acquired through the third technique, behave in a decreasing manner on InGaN layer in terms of picometer and they behave in a manner that initially increases and later on decreases for the AlGaN layer. The correction function on the third technique cannot be used for *a* lattice parameter and it behaves in a manner that initially increases and later on decreases for both the InGaN and the AlGaN layers depending on the growth temperature.

**Table 1.** The lattice parameters found through Vegard, universal lattice parameters and cubical equations on InGaN and AlGaN layers for all samples and their comparisons.

| InGaN/ AlGaN | T °C | $c_{vegard}$ nm | $c_o$ nm | $c_{err.}$ nm | $a_{vegard}$ nm | $a_o$ nm | $a_{err.}$ nm |
|---|---|---|---|---|---|---|---|
| **A** | 650 | 0.5231/ 0.5139 | 0.5228/ 0.5141 | 0.5231/ 0.5139 | 0.3207/ 0.3168 | 0.3215/ 0.3163 | 0.3139/ 0.3222 |
| **B** | 667 | 0.5230/ 0.5145 | 0.5226/ 0.5147 | 0.5230/ 0.5145 | 0.3202/ 0.3171 | 0.3214/ 0.3166 | 0.3097/ 0.3219 |
| **C** | 700 | 0.5223/ 0.5123 | 0.5225/ 0.5129 | 0.5223/ 0.5123 | 0.3217/ 0.3176 | 0.3213/ 0.3156 | 0.3248/ 0.3373 |

The point and line defects of GaN layer cause directional shifts on the lattice, and the shift leads to minute deviations on the peak. The distance between the strained planes is directly related to the lattice parameters and to the ratio of In. Also, the strain risen as the polar angle increases and the square of the sinus of the angle provide a definition for the strains on the lattice. The strain on InGaN and AlGaN alloys is biaxial (two-directional), and they might cause strains that are either positive or negative. If these strains are gradient, they must have three axes, and in this case there must be a component of the surface-normal strain. Strain can be calculated through the baseplate or through its universal values. Here, the strain value is calculated for the universal values of InGaN and AlGaN. The strain equation can be given as;

$$\frac{\delta d}{d}, \frac{\delta a}{a}, \frac{\delta c}{c} = -\delta\,\theta\,Cot\,\theta \quad (5)$$

with its error function [18].

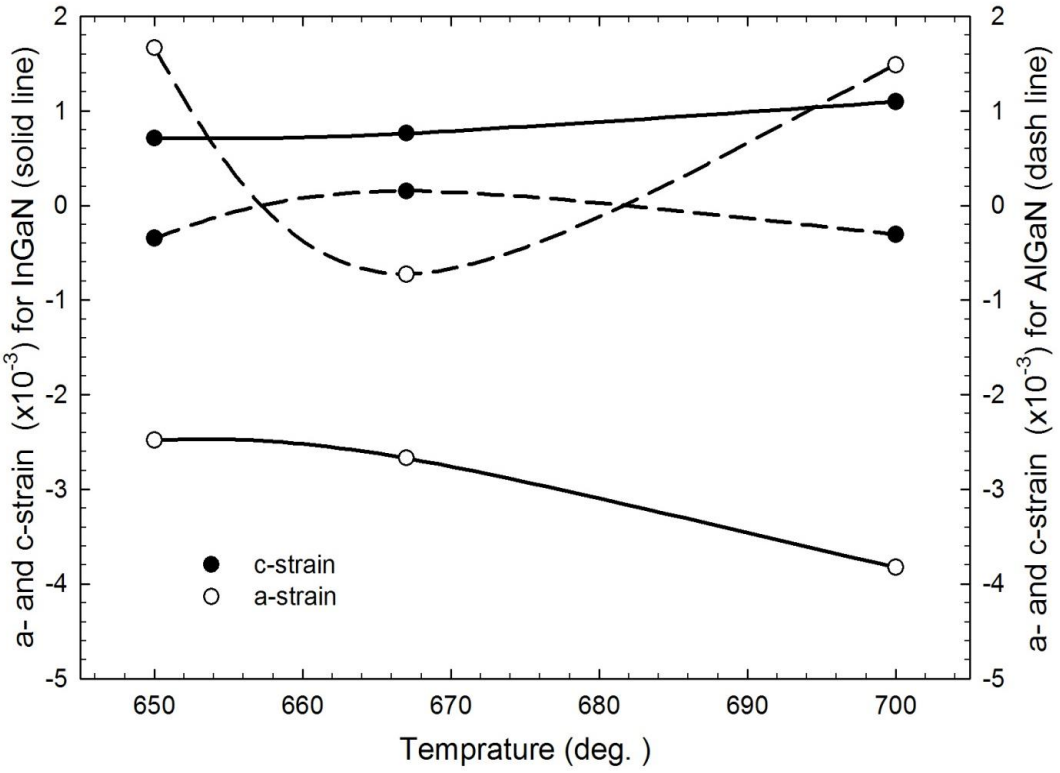


**Figure 4.** The temperature-dependent *a*- and *c*- lattice strain of all the samples on InGaN and AlGaN layer.

On Figure 4, the *a*- and *c*- strains on the layers depending on the growth temperatures are given. Solid lines represent InGaN while the dashed lines represent AlGaN layer. As given on Figure 4, with the increasing growth temperature, the strain *c* increases on InGaN layer when strain *a* decrease on the negative value. On AlGaN layer, while Strain *c* behaves in a manner that initially increases and later on decreases, Strain *a* acts in a completely opposite manner. The vast difference in the increase-decrease or decrease-increase behavior of AlGaN is related to strains caused by the abrupt cooling of Al structure. The increase or decrease of the strain values of InGaN layer, which are close to be linear, shows that the point defects don't create dramatic effects on this layer. Additionally, as it can be seen on Figure 4, InGaN layers, the strain values of InGaN layer on asymmetrical planes are lower. This indicates that the quality of the structure is quite well.

According to the Vegard Law, the ratio of the alloy on InGaN layer is dependent onto the peak positions of InN and GaN. The existence of deviations outside the expected percentage of the peak of these two layers on InGaN reveals the existence of the strain. When the *x* value of InGaN is different from what it is supposed to be, it is calculated through the Vegard Law. However, in order to differentiate the strain value appendage of InGaN at *x* value, the cubical equation of $Ax^3 + Bx^2 + Cx + D = 0$ can be used [20]. A, B, C and D coefficients of this cubical equation includes InN, universal *a* and *c* lattice parameters of GaN and Poission ratios, and it is acquired by means of using lattice parameters, Vegard Law and Poission Equation. The *x* ratio can be solved with the aid of a programme in 0-1 interval, and qualities such as strain and relax are calculated afterwards. The calculated *x* values of InGaN for increasing temperature are % 10.87, 9.01, 7.51 consecutively. Through the *x* ratio that has been found; strain, hydrostatic and biaxial strain values can be calculated correctly.

On two dimensions, biaxial strain is known as lattice compression or tensile. Lattice strain is the sum of the biaxial strain components on two dimensions, and it is the sum of the hydrostatic components on three dimensions. The components of biaxial and hydrostatic strain are as follows [16,21,22];

$$\varepsilon_c = \varepsilon_c^b + \varepsilon_h, \quad \varepsilon_a = \varepsilon_a^b + \varepsilon_h \tag{6}$$

$$\varepsilon_h = \frac{c_{33}\varepsilon_c + 2c_{13}\varepsilon_a}{2c_{13} + c_{33}} \tag{7}$$

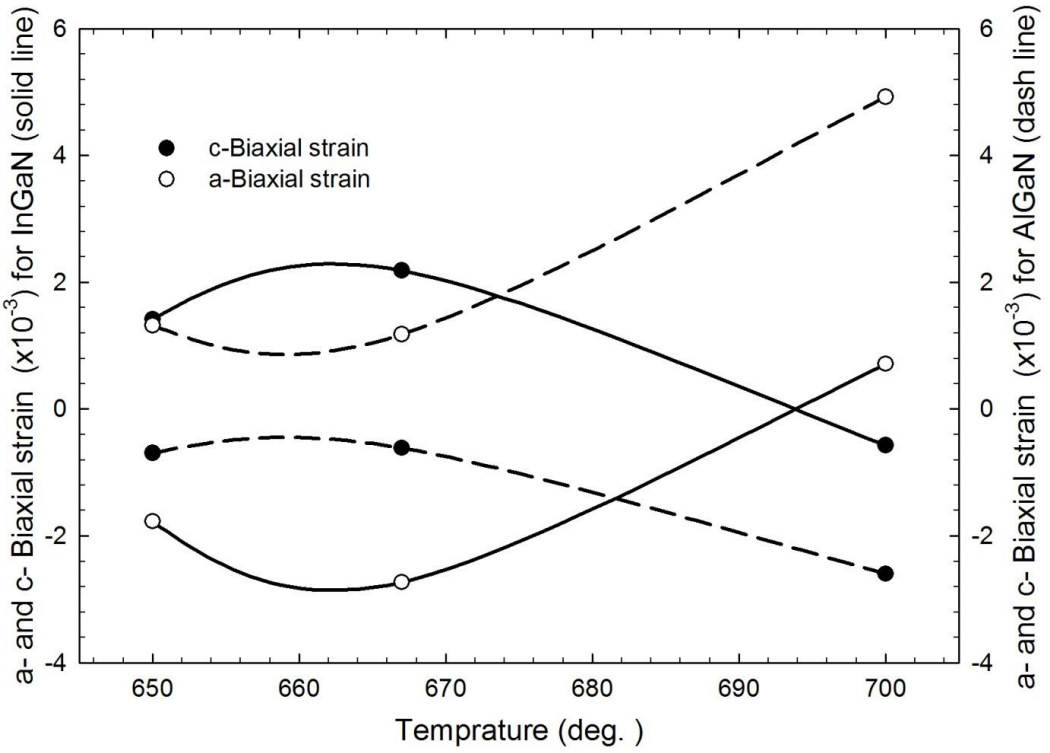


**Figure 5.** Temperature-dependent a- and c- biaxial strains for all samples on InGaN and AlGaN layers.

On Figure 5, *a*- and *c*-biaxial strains of layers for the increasing growth temperature are given. These biaxial strain values are calculated through the normal strain values of Equation 6 and the calculated hydrostatic strain values. On Figure 5, the solid lines represent InGaN and the dashed lines represent AlGaN layer. In a paralleling manner, on both InGaN and AlGaN layers, biaxial strain *c* initially increases and later on decreases when biaxial strain *a* acts in the opposite way as the growth temperature of the active layer increases. Kachkanov et. al. suggest that the strain, which dominates the microcrystal ensembles, originates from intrinsic residual stress generated in microcrystals [23]. On the epitaxial layer, the internal plane strain can be calculated using the equations below, if the a-biaxial strain and the material elasticity constants are known. [22,24]

$$\sigma_f = \left( c_{11} + c_{12} - 2\frac{c_{13}^2}{c_{33}} \right) \varepsilon_a^b \qquad (8)$$

Here, the information in the parenthesis is labeled as biaxial module ($M_f$); hence the biaxial strain is shown with $\sigma_f = M_f \varepsilon_a^b$ [22,23].

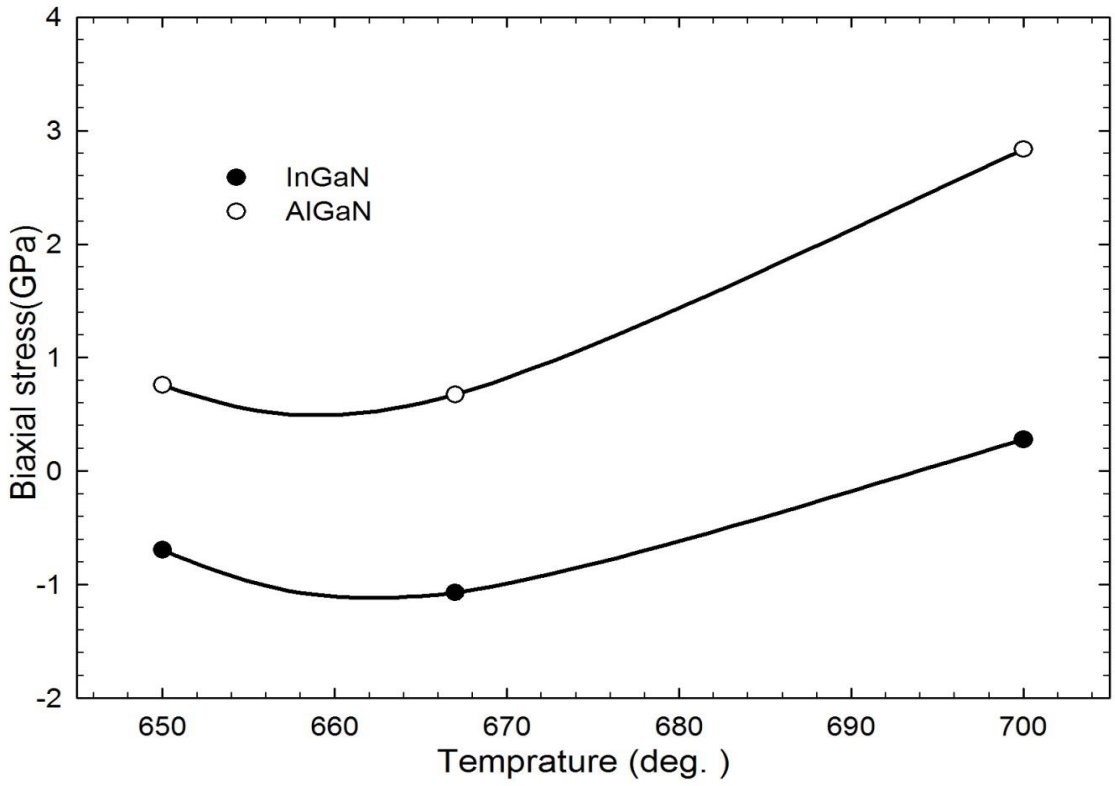


**Figure 6.** The temperature-dependent biaxial strain of InGaN and AlGaN layers in InGaN MQW blue LED structures.

The biaxial strains, which are calculated for all the samples, are given as dependent onto the temperature on Figure 6. As it can be seen on the Figure, while only the layer of InGaN that has been grown at 667 $^{o}$C has compressive biaxial strain, all the other sample planes display tensile strain qualities. Besides, depending on the increasing temperature, even when the strain qualities display initially increasing and later on decreasing behavior on both layers, the biaxial strain values of AlGaN are higher compared to those of InGaN. The reason for this difference is that the thermal growth constant difference between AlGaN and InGaN layers is higher than that of InGaN and GaN layers [14].

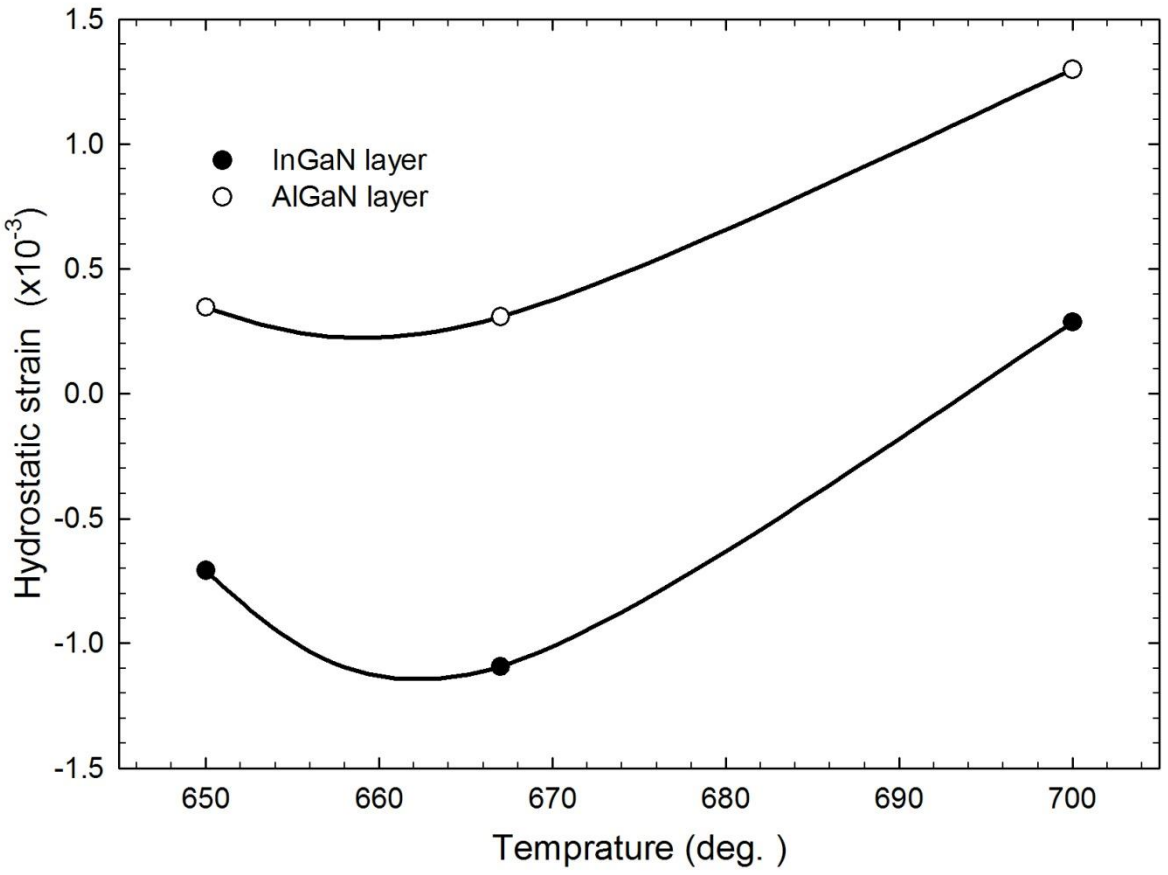


**Figure 7**. The temperature-dependent hydrostatic strain of all the samples at InGaN and AlGaN layers.

On Figure 7, it can be seen that the hydrostatic strain values are displaying initially decreasing and later on increasing behavior on the negative values of InGaN layer and on the positive values of AlGaN layer depending on the increasing layer growth temperatures. While that leads to stressing of the hydrostatic strain on InGaN layer, it leads to tensing of the hydrostatic strains on AlGaN layer in the same trend. Such defects display paralleling behaviors for both planes.

On hydrostatic strain alloy structures, it is affected by doping and point defects. Depending on the size of the strain defects, the lattice can be compression or tensile. Different types of point defects might emerge depending on the growth conditions. In general, it can be expected that the effective hydrostatic strain in GaN originates from $Al_{Ga}$, $Ga_N$, $N_{In}$, $Al_N$, $Ga_{In,}$ $N_{Ga}$ and $Ga_N$ substitutional type point defects, $N_i$, $Ga_i$, $Al_i$, and $In_i$ interstitial point defects, and $V_{Al}$, $V_N$, $V_{In}$ and $V_{Ga}$ vacancies [13,25]. The covalent radius of the Al(1.43Å), Ga(1.22 Å) and In(1.63 Å) atoms are considerably larger than the covalent radius of the N(0.70 Å) atom. Covalent values can be found easy from textbooks or other way. Therefore, $Al_{Ga}$, $Ga_N$ $In_N$, $Al_N$, $In_{Ga}$, $In_{Al,}$ $In_i$, $Ga_i$, $Al_i$ and $N_i$ type defects cause a crystal lattice expansion, whereas $Ga_{Al}$, $N_{Ga}$, $N_{In}$, $N_{Al}$, $Ga_{In}$, $AlI_{n,}$ $V_{Al}$, $V_{Ga}$, $V_{In}$, and $V_N$ type point defects lead to crystal lattice compression. In our case, we find that the hydrostatic strain in first two temperature values of the InGaN layer is of compressive character and large by absolute value (see Figure 7). Therefore, we suppose that in the films the relative concentrations of $Ga_{Al}$, $N_{Ga}$, $N_{In}$, $N_{Al}$, $Ga_{In}$, $AlI_{n,}$ $V_{Al}$, $V_{Ga}$, $V_{In}$, and $V_N$ type defects are dominant with respect to other types of point defects. But in increasing temperatures, hydrostatic strain of InGaN converts from lattice compressive to expansion behavior; therefore, the $Al_{Ga}$, $Ga_N$ $In_N$, $Al_N$, $In_{Ga}$, $In_{Al,}$ $In_i$, $Ga_i$, $Al_i$ and $N_i$ type defects dominate InGaN. In AlGaN layes, this strain type exhibits complete lattice expansion behavior, and other type of defects including vacancies become dominant in character. The biggest absolute value of hydrostatic strain is determined for the InGaN at 667$^o$C and AlGaN at 700$^o$C, which exhibits, on the whole, extreme deformation behavior with big concentration of point defects, but the case of smallest absolute value of hydrostatic strain with the closer the lattice parameter to universal lattice parameters and the most favorable condition take place for coherent growth of layers.

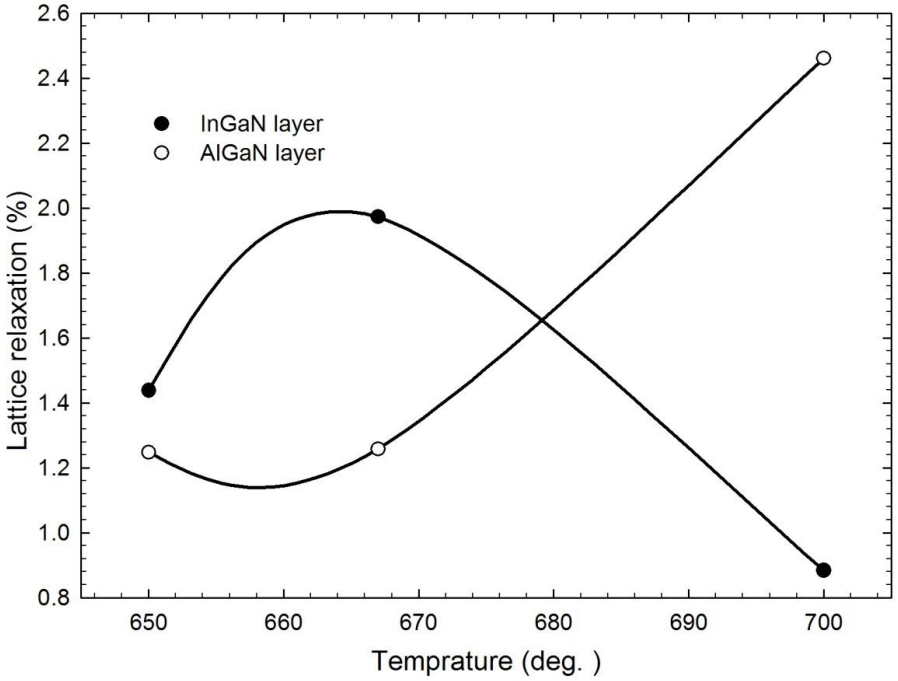


**Figure 8**. Temperature-dependent lattice relax of all samples on InGaN and AlGaN layers.

Lattice relaxation is defined as the percentage of the ratio of the difference of relaxed lattice length between layers and substrate layers to the difference of universal lattice lengths, and it is represented with the equation below [18];

$$R_{\%} = \frac{a_{\parallel}^{L(means)} - a_{\parallel}^{S(means)}}{a_{\parallel}^{L(0)} - a_{\parallel}^{S(0)}} x100 \quad (9)$$

The calculated temperature-dependent lattice relaxation of InGaN and AlGaN layers is given on Figure 8. While the lattice relaxation initially increases and later on decreases on InGaN layer due to the increasing growth temperature, on AlGaN layer, it behaves on the exact opposite manner. Up to 667 $^{o}$C, the lattice relaxation value of InGaN is higher than the lattice relaxing value of AlGaN; however, the relaxation level at increasing temperature has been higher for AlGaN layer afterwards. The result clearly shows that 667 $^{o}$C is the optimum growth temperature for InGaN blue LED structure.

## 4. CONCLUSION

In this study, three MQW InGaN LED structures with five periods each have been grown at 650 $^{o}$C, 667 $^{o}$C and 700 $^{o}$C active layer temperatures through the MOCVD technique. All analyses of the structures have been completed through the reciprocal lattice space mapping measured by HRXRD. It has been identified that the crystal qualities are better than InGaN peak half-widths at the growth temperature of 667 $^{o}$C. When the FWHM values are compared, it can be seen that the crystal quality of AlGaN is lower than that of InGaN. In this study, In alloy ratio of InGaN has ben found through cubical equations, and the In ratios calculated through Vegard Law are compared to lattice lengths calculated afterwards. Consecutively, the *x* values for InGaN can be listed as %10.87, 9.01, 7.51. The lattice parameters calculated using Vegard and cubical equations generally differed on the third decimal, and this difference is calculated as the strain value. Strain, hydrostatic strain, biaxial strain and normal strain values are characteristically similar to the calculated In *x* ratios. While the hydrostatic strain is lattice compressive volumetric deformation on samples whose growth temperatures are 650 $^{o}$C and 667 $^{o}$C, it is lattice tensile volumetric deformation on the sample whose growth temperature is 700 $^{o}$C on InGaN MQW layer. Substitutional and vacancies type point defects can be seen on the first two growth temperatures (650 and 667 $^{o}$C) on InGaN layer, and the substitutional and interstitial type point defects are common on both high growth temperatures of InGaN and on all the samples grown on all temperatures of AlGaN. It has been seen that the InGaN layer has less defects at a temperature of 667 $^{o}$C in terms of *a*-biaxial strain, biaxial strain, lattice relaxation and hydrostatic strain. Even though AlGaN layer is more relaxed at this temperature, biaxial strain and strain levels are less pronounced. As a result, the sample that has been studied at the growth temperature of 667 $^{o}$C is ideal for MQW blue LED designs due to the lessened point defect qualities. Finally, the less

defected samples can be suitable for the rise of the quality of white LEDs.

**ACKNOWLEDGMENTS**

This work was supported by DPT under the project no. 2011K120290 and by BAP at Gazi Univ. under project no. 05/2009-58.

**CONFLICT OF INTEREST**

No conflict of interest was declared by the authors.

**REFERENCES**

1. High-Brightness LED Market Review and Forecast 2007, Published: Strategies Unlimited 2007.
2. M. K. Öztürk, S. Çörekçi, M. Tamer, S. Ş. Çetin, S. Özçelik, E. Özbay Applied Physics A-Materials Science&Processing, 114, 1215-1221 (2014).
3. M.K. Öztürk, E. Arslan, İ. Kars, S. Özçelik, E. Özbay, Materials science in semiconductor processing, 16, 83-88 (2013).
4. S. Çörekçi, M.K. Öztürk, Y. Hongbo, M. Çakmak, S. Özcelik, E.Özbay, Semiconductors, 47, 820-824 (2013).
5. S. Nakamura, Science, 281, 956 (1998).
6. S. Nakamura, M. Senoh, S. Nagahama, N. Iwasa, T. Matsushita, T. Mukai, Appl. Phys. Lett. 76, 22-24 (2000).
7. S.S. Cetin, M.K. Öztürk, S. Özçelik, E. Özbay, Crystal Research and Technology, 47(8), 824-833 (2012).
8. S. Korçak, M.K. Öztürk, S. Çörekçi, B. Akaoğlu, Y. Hongbo, M. Çakmak, S. Sağlam, S. Özcelik, E.Özbay, Surface Science, 601, 3892-3897 (2007).
9. J.H. Ryou, W. Lee, J. Limb, D. Yoo, J.P. Liu, R.D. Dupuis, Z.H. Wu, A.M. Fischer, F.A. Ponce, Appl. Phys. Lett. 92, 101113:1-3 (2008).
10. A.Yıldız, M.K. Öztürk, M. Bosi, S. Özçelik, M. Kasap, Chinese Phys. B 18(9), 4007-4012 (2009).
11. Krost, A. Dadgar, G. Strassburger, R. Clos, Phys. Stat. Sol. (a) 200(1), 26-35 (2003).
12. M.K. Öztürk, Y. Hongbo, B. Sarikavak, S. Korcak, S. Özçelik, E. Özbay, J. Mater. Sci: Mater. Electron., 21 (2), 185-191 (2010).
13. Kisielowski, J. Kruger, S. Ruvimov, T. Suski, J.W. Ager, E. Jones, Z. Liliental-Weber, M. Rubin, E.R. Weber, M.D. Bremser, R.F. Davis, Phys. Rev. B 54, 17745-17753 (1996).
14. M.K. Öztürk, H. Altuntaş¸ S. Çörekçi, Y. Hongbo, S. Özçelik and E. Özbay, 47, 19-27 (2011).
15. Baş, Y., Demirel, P., Akın, N., .Başköse, C., Özen, Y., Kınacı B., Öztürk, M.K., Özçelik, S. and Özbay, E. (2014). Microstructural defect properties of InGaN/GaN blue light emitting diode structures. *Journal of Materials Science: Materials in Electronics*, 25(9), 3924-3932.
16. Kisielowski, Semicon. Semimet., 57, 275-317 (1999).
17. Wassermann G and Grewen J 1962 Texturen metallischer Werkstoffe (Berlin: Springer) pp 754–5
18. M. A. Moram and M. E. Vickers, Rep. Prog. Phys., 72, 036502 (2009).
19. Suryanarayana, M.G. Norton, X-Ray Diffraction: A practical Approach, Plenum Press, New York, 1998.
20. M. Schuster, P. O. Gervais, B. Jobst, W. Ho¨sler, R. Averbeck, H. Riechert, A. Iberlk and R. Sto¨mmerk, J. Phys. D: Appl. Phys. 32, 56 (1999).
21. S.I. Cho, K. Chang, M.S. Kwon, J. Mater. Sci., 43, 406-408 (2008).
22. V.S. Harutyunyan, A.P. Aivazyan, E.R. Weber, Y. Kim, Y. Park, S.G. Subramanya, J. Phys. D: Appl. Phys., 34, A35-A39 (2001).
23. V. Kachkanov B. Leung, J. Song, Y. Zhang, M.-C. Tsai, G. Yuan, J. Han2 & K. P. O'Donnell, Scientific Reports, 4, 4651, (2014).
24. M.A.G. Halliwell, J. Cryst. Growth, 170, 47-54 (1997).
25. S.I. Cho, K. Chang, M.S. Kwon, J. Mater. Sci., 42, 3569-3572 (2007).